Non-Confocal 3D Reconstruction in Volumetric Scattering Scenario

Dongyu Du , Xin Jin , *Senior Member, IEEE*, and Rujia Deng

Abstract—Real-time scattering imaging technology is of great importance for transportation in extreme weather, scientific research in the deep ocean, emergency rescue in heavy smoke, and so on. Among existing volumetric scattering imaging methods, time-of-flight (ToF) methods based on confocal imaging architecture, isolating or modeling scattering photons, present the best visual reconstruction ability. However, these methods rely on the long acquisition time to capture more effective photons and thus fail to deal with real-time imaging tasks. In this article, aiming at providing both high-speed and high-quality scattering reconstruction, a dual optical coupling scattering transmission model is proposed to accurately describe the spatial and temporal propagation of scattered photons in the non-confocal imaging architecture. Then, a non-confocal boundary migration model (NBMM) is designed to establish the mapping between scattered measurement and object information. Besides, using the special characteristic of the temporal transfer matrix, a depth reconstruction method based on re-focusing is developed to recover the 3D structure of the object. Finally, a non-confocal imaging system is built to capture photons for all pixels simultaneously and verify the effectiveness of the proposed method. The experimental results show that the proposed method can recover 3D objects located at a one-way scattering length of 22.2 transport mean free paths (TMFPs), corresponding to the round-trip scattering length of 44.4 TMFPs, which is 6.9 times more than typical non-confocal methods. It operates 600 times faster than confocal methods and only requires 100 ms exposure time, which is very beneficial to a variety of real-time scattering applications.

Index Terms—Volumetric scattering imaging, time-of-flight, diffuse optical tomography.

I. INTRODUCTION

IMPROVING the imaging ability in the volumetric scattering media is of great importance for existing imaging devices to operate well in challenging environmental conditions. For example, seeing in the clouds, fog, haze, or turbid water is crucial to the navigation system and remote sensing [1], [2], [3], [4], [5], [6]; imaging through the tissue to obtain high-resolution images is also desired for medical diagnosis and treatment [7], [8].

Significant effort has been dedicated to improving the reconstruction quality in the volumetric scattering scenarios. Among these methods, some time-of-flight active methods [9], [10] utilize the properties of scattered photons and accurately model the spatial-temporal scattering propagation process and thus provide the best reconstruction performance in the highly scattering scenario. However, these methods require the scenario to be scanned using a confocal imaging system to capture more effective photons, resulting in a long acquisition time of tens of minutes or seconds which is not acceptable in real-time applications. Additionally, in the confocal imaging system, the single-pixel ultrafast sensor is focused on the same point as the scanned pulsed laser, which disregards the light that reflects off the other pixels' positions in the scenario. Some other works have reduced acquisition time to a few seconds by using an ultrafast detector array. However, due to the limited utilization of the properties of scattered photons and approximate modeling of complex scattering propagation in non-confocal architecture, these methods can only handle weak scattering cases [4], [11], [12], [13], [14] or recover simple 2D objects [15]. Therefore, breaking the inherent constraint between scattering imaging capability and acquisition complexity is challenging.

To address this problem, in this article, we design a non-confocal imaging system alongside a non-confocal imaging model and reconstruction method, which adequately harness and accurately model all photons returned from the scenario and thus enable high-quality and high-speed reconstruction in highly scattering scenarios. The experiments verify that the scattering reconstruction capability of the proposed method is 6.9 times more than that of the existing non-confocal scattering method. Compared with confocal scattering methods, the proposed method significantly reduces the acquisition time from tens of minutes to a millisecond level without large degradation of imaging quality and scattering imaging capability. We believe that the proposed method paves the way toward real-world imaging in the extreme scattering scenario.

The remainder of this article is organized as follows. Section II introduces the related works. Section III derives the proposed dual optical coupling scattering transmission model, non-confocal boundary migration model, and depth reconstruction method in detail. The experimental setup, reconstruction results under the static and dynamic scattering scenarios, and performance analysis are provided in Section IV. Conclusions are drawn in Section V.

Dongyu Du and Rujia Deng are with the Shenzhen International Graduate School, Tsinghua University, Shenzhen 518055, China, and also with the Tsinghua Innovation Center in Zhuhai, Zhuhai 519080, China (e-mail: dudy19@mails.tsinghua.edu.cn; drj20@mails.tsinghua.edu.cn).

Xin Jin is with the Shenzhen International Graduate School, Tsinghua University, Shenzhen 518055, China (e-mail: jin.xin@sz.tsinghua.edu.cn).

II. RELATED WORKS

Active imaging systems show the best scattering imaging capability since they can record both spatial and temporal interaction between the photons and the scattering scenario by emitting light from a pulsed laser and measuring the time-of-flight information using an ultrafast detector. In this section, we review the existing time-of-flight scattering imaging methods and the corresponding scattering imaging system architecture.

A. Time-of-Flight Volumetric Scattering Imaging Methods

Time-of-flight-based scattering imaging methods try to recover the object information by extracting ballistic photons or modeling scattered photons. Isolating ballistic photons can be achieved by temporal filtering, parametric fitting, or cross-correlation. Temporal filtering methods [11], [12], [14], [16], [17] design a time-gating mechanism as a prior of the object depth to extract ballistic photons. Parametric fitting methods [4], [18], [19], [20] model the statistical distribution of ballistic and scattered photons and fit the measured time profile to distinguish the temporal distribution of ballistic photons. Calculating the cross-correlation [13], [21], [22] between the measurements and instrumental responses can also enhance the effect of ballistic photons. These methods have low computational complexity while they are infeasible in highly scattering scenarios where the ballistic photons are greatly attenuated and highly coupled with scattered photons.

Different from the above methods which extract ballistic photons, some methods theoretically model the spatial-temporal propagation of scattered photons and invert the forward imaging model to reconstruct the object. However, inverting the scattering imaging models, such as the radiative transfer equation (RTE) or diffusion equation (DE), is inherently ill-posed and highly undetermined. To address this problem, diffuse optical tomography (DOT) methods [23], [24], [25] make some specific assumptions to obtain the analytical solution, resulting in low-resolution reconstructions. Additionally, these methods rely on multiple source-detector pairs to alleviate the ill condition of the inverse problem, which increases the acquisition complexity. Lyons et al. [15] proposed an optimization framework to solve the scattering model in optical transmission mode. While this method can operate well in highly scattering scenarios, it can only recover 2D objects with the object depth and the thickness of the scattering media as priors. Besides, limited by the heavy computation workload, it suffers from a low reconstruction quality and long computation time. In our previous work [10], we provided an efficient solution without computational approximation and demonstrated the high-quality reconstruction in the highly scattering media with a one-way scattering length of 25.4 TMFPs, while it requires scanning the scenario by using a confocal imaging system, resulting in a long acquisition time.

B. Volumetric Scattering Imaging System Architecture

According to the cooperation mode of laser and detector, existing time-of-flight imaging systems can be divided into confocal and non-confocal imaging systems. In the confocal imaging system, a pulsed laser illuminates a point in the scenario and the single-pixel ultrafast detector focuses on the same point. The measurements are collected by changing the scanning point. Since the laser power is concentrated in this case, more effective signal photons can be captured, which is conducive to the scattering reconstruction. Additionally, the confocal acquisition procedure provides some specific optical path constraints, which can be used to simplify the scattering imaging model [9], [10]. Therefore, the confocal system allows high-quality reconstruction while the scanning mechanism results in a long acquisition time which is not acceptable in real-time applications. In contrast, the non-confocal imaging system is based on the multi-pixel detector array which can capture photons for all pixels simultaneously and thus greatly shorten the acquisition time. However, modeling the scattering propagation in the non-confocal architecture is challenging since the detector captures photons that reflect off the other pixels' positions in the scenario, which breaks the key assumption about optical paths in confocal systems. Besides, the laser power is dispersed in the non-confocal system, which reduces the amount of captured signal photons and further hinders the reconstruction. Therefore, existing non-confocal methods simply isolate the ballistic photons or build the model in the restricted scenario so that they can only handle the weak scattering scenarios [4], [11], [12], [13], [14] or recover the simple 2D object [15].

Overall, existing volumetric scattering methods operate in a tradeoff between the scattering imaging capability and the acquisition complexity. To provide both high-speed and high-quality target recovery in the highly scattering scenarios, in this article, a non-confocal imaging system is built to provide fast acquisition; a dual optical path coupling scattering transmission model is proposed to accurately describe the propagation of scattered photons in the non-confocal system; a non-confocal boundary migration model and a depth reconstruction algorithm is designed to achieve high-quality target recovery.

III. THE PROPOSED NON-CONFOCAL SCATTERING IMAGING MODEL AND RECONSTRUCTION METHOD

The proposed non-confocal scattering imaging model and reconstruction method are based on the non-confocal time-of-flight imaging system, as illustrated in Fig. 1. The imaging target is embedded in the volumetric scattering media. The divergence of the pulsed laser is expanded by a diffuser to illuminate the entire volumetric scattering scenario. The ultrafast detector array records the time-of-flight information of photons that diffuse through the volumetric scattering region and scatter back from the hidden objects and scattering media. The 3D measurement is generated with a single exposure using a non-confocal imaging system.

In order to recover the object from the measurements with ultra-incomplete optical signals, we first propose a dual optical path coupling scattering transmission model to forward describe the propagation of scattered light in the non-confocal system, as detailed in Section A. Then, a non-confocal boundary migration algorithm is developed to inverse the forward imaging formation
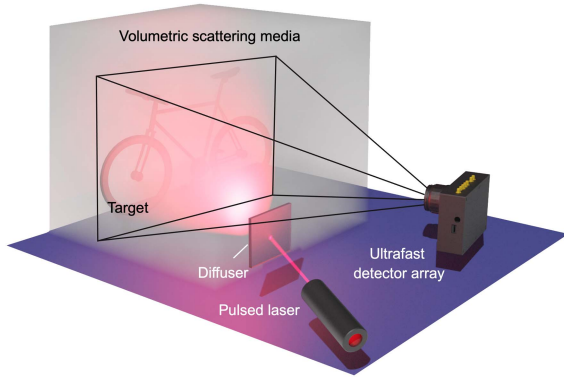
Fig. 1. Schematic diagram of non-confocal time-of-flight imaging system. The object is embedded in the volumetric scattering media. A pulse laser emits the light that passes through the diffuser and illuminates the entire scenario. An ultrafast detector captures the light for all pixels simultaneously without scanning and generates the measurement which records the spatial and temporal information of the photons.

model and recover the hidden object, as detailed in Section B. Finally, a depth reconstruction method is designed to achieve 3D reconstruction, as detailed in Section C. During the derivation, we make several assumptions: the scattering medium is homogenous so that its characteristics are spatially invariant; the surface structure of the object does not introduce extra optical paths; partial occlusions within hidden scene parts are ignored; multi-bounce transport between objects is neglected.

A. Dual Optical Path Coupling Scattering Transmission Model

We first model the propagation process of the scattered photons in the non-confocal imaging system and describe it as:

$$Y = A(O) + W, \quad (1)$$

where $Y \in \mathbb{R}^{M \times M \times T}$ is the spatial-temporal measurements with $M \times M$ pixel size and T time bins; $O \in \mathbb{R}^{X \times Y \times Z}$ is the hidden object with a size of $X \times Y \times Z$; $A: \mathbb{R}^{X \times Y \times Z} \rightarrow \mathbb{R}^{M \times M \times T}$ is the mapping operator from the object to the 3D measurements; and W represents the additive random noise. Different from the confocal system where the illumination source and detector share an optical path so that the confocal mapping operator is established based on a single optical path, that is, directly between the object and the detector, the light propagation in the non-confocal system cannot be simplified as a one-way propagation. In this case, to computationally describe the mapping in (1), we model the propagation of scattered photons in the non-confocal imaging system as a dual optical path coupling process, as shown in Fig. 2(a): the incident light forward propagates to the object, then the scattered light is reflected by the object and backward propagates to the detector. The forward scattered field is denoted as $\phi_i(x, y, z, t)$, which represents the electromagnetic radiation in the 3D space (x, y, z) and time t and is physically equivalent to the photon fluence rate. The propagation direction and intensity of photons after they hit a point on the object is described by a function $g(x, y, z)$, which incorporates the surface characteristics of the object such as albedo, surface normal, bidirectional scattering distribution

function (BSDF) and so on. The backward scattered field is denoted as $\phi_e(x, y, z, t)$. The above mathematical symbols are also instructed in Fig. 2(a). Assuming the surface structure of the object does not introduce an extra optical path, i.e., the depth difference of the object is ignored, the spatial variability in the depth dimension of the scattered field caused by the object can be neglected. Then the mapping operator can be described in terms of convolution, which is as follows:

$$A(\cdot) = [\phi_i(x, y, z, t) \times g_T(x, y, z)] * \phi_e(x, y, z, t), \quad (2)$$

where $*$ indicates a convolution and $g_T(x, y, z)$ is constructed by repeating the $g(x, y, z)$ in the fourth dimension T times. The time-resolved diffusion equation is used to analytically describe the forward and backward scattered fields. In this case, the $\phi_i(x, y, z, t)$ and $\phi_e(x, y, z, t)$ satisfy the following differential equations:

$$\begin{cases} \frac{1}{c} \frac{\partial \phi_i(x,y,z,t)}{\partial t} - D\nabla \cdot [\nabla \phi_i(x, y, z, t)] + \mu_a \phi_i(x, y, z, t) \\ \quad = s(x, y, z, t), \\ \frac{1}{c} \frac{\partial \phi_e(x,y,z,t)}{\partial t} - D\nabla \cdot [\nabla \phi_e(x, y, z, t)] + \mu_a \phi_e(x, y, z, t) \\ \quad = \phi_i(x, y, z, t) \cdot g_T(x, y, z), \end{cases}$$

$$(3)$$

where c is the speed of light in the medium; D is the diffusion coefficient which includes the absorption coefficient μ_a and the reduced scattering coefficient μ_s' and is given by $D = (3(\mu_a + \mu_s'))^{-1}$; $s(x, y, z, t)$ is the incident light source which is approximated as an infinite area light here.

Combining the (1)–(3), the scattering transmission model in the non-confocal imaging system, i.e., the forward non-confocal imaging model, can be obtained. The mapping between the measurements and the object is also implicitly given.

B. Non-Confocal Boundary Migration Model

Unfortunately, it is computationally infeasible to directly compute the mapping operator (2) and further invert the forward imaging model to reconstruct the hidden object. To address this problem, a non-confocal boundary migration model is proposed to transform the inverse problem into a boundary migration problem. First, without loss of generality, the measurements Y can be expressed as the spatial boundary of the backward scattered field after calibrating the distance among the laser, the detector, and the front surface of the scattering media, i.e., $Y = \phi_e(x, y, z = 0, t)$. Photons propagate forward toward the object while assuming that the surface structure of the object does not introduce extra optical paths, then the difference in the arrival time of these photons at the object's surface can be neglected. In this case, the origin of the backward scattered field is approximated as the steady state field in the time domain. Therefore, the temporal boundary of the backward scattered field can be denoted as the time integral of the forward scattered field changed by the object:

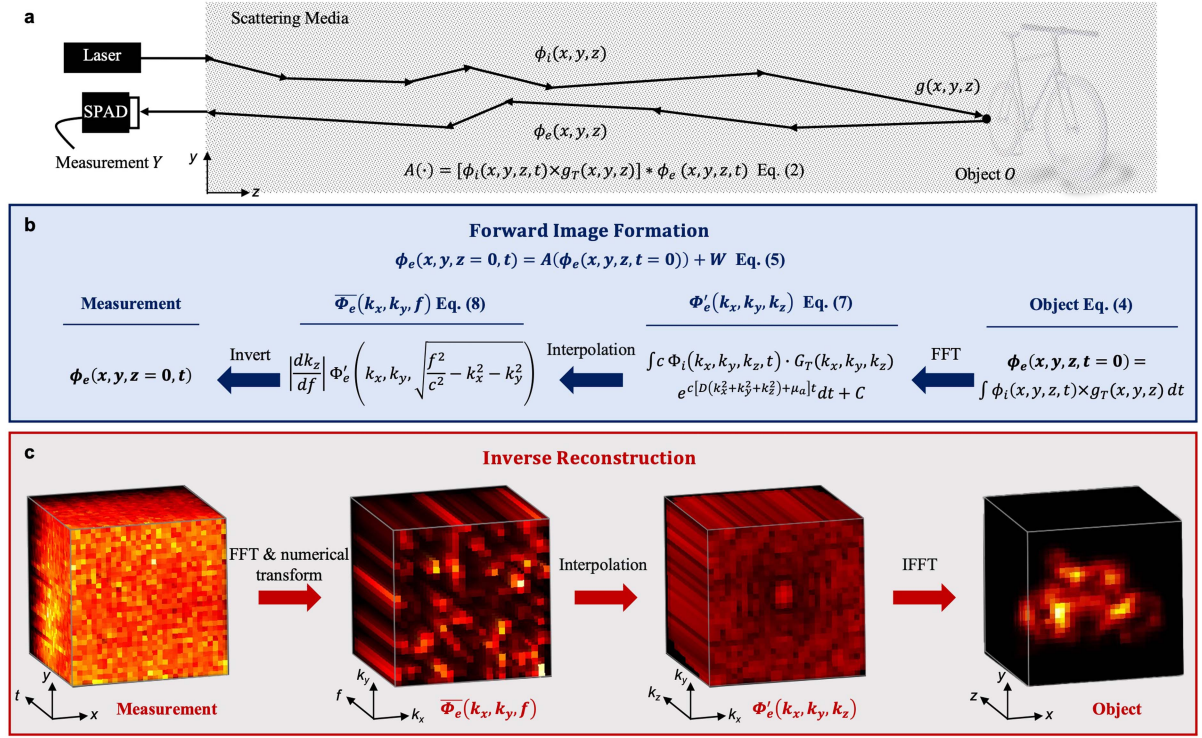$$\phi_e(x, y, z, t = 0) = \int \phi_i(x, y, z, t) \times g_T(x, y, z) \, dt, \quad (4)$$

Fig. 2. Schematic diagram of non-confocal light propagation and pipelines of forward image formation and inverse reconstruction. (a) A pulsed laser emits the light into the scattering scenarios. The photons are forward scattered to the object O and backscattered to the detector. The detector (SPAD) captures the scattered photons to generate the measurement Y. The forward and backward scattered fields are denoted as $\phi_i(x, y, z)$ and $\phi_e(x, y, z)$. The function $g(x, y, z)$ describes the object's surface characteristics. (b) The non-confocal forward image formation pipeline from object, $\Phi'_e(k_x, k_y, k_z), \overline{\Phi_e}(k_x, k_y, f)$, to measurement. (c) The pipeline of inverse reconstruction from measurement, $\overline{\Phi_e}(k_x, k_y, f), \Phi'_e(k_x, k_y, k_z)$ to object.

which is different from the confocal method that treats the virtual illumination of the object as the temporal origin of the scattered field. Since the field $\phi_e(x, y, z, t = 0)$ represents the main characteristics of the object, the object can be approximated as the temporal boundary of the backward scattered field, i.e., $O = \phi_e(x, y, z, t = 0)$. Then, combining the temporal boundary shown in (4) and the spatial boundary given by the position of the detector, the non-confocal forward imaging formation model (1) can be expressed as:

$$\phi_e\left(x, y, z = 0, t\right) = A\left(\phi_e\left(x, y, z, t = 0\right)\right) + W. \quad (5)$$

The mapping operator $A(\cdot)$ represents the space-to-time transformation of the backward scattered field $\phi_e(x, y, z, t)$. In this case, $A(\cdot)$ does not need to be computed analytically and can be computationally achieved by extending the confocal boundary migration model [10]. The mapping process from object to measurement is derived below and the corresponding pipeline is shown in Fig. 2(b). Based on the second differential equation of (3), the spectrum of backward scattered field $\phi_e(x, y, z, t)$ on the spatial dimensions over (x, y, z) can be derived as:

$$
\begin{aligned}
&\phi_e\left(x, y, z, t\right) \\
&= \frac{1}{(2\pi)^3} \iiint \Phi_e\left(k_x, k_y, k_z, t\right) e^{i(k_x x + k_y y + k_z z)} dk_x dk_y dk_z,
\end{aligned}
\quad (6)
$$

where

$$
\begin{aligned}
\Phi_e\left(k_x, k_y, k_z, t\right) = & \, e^{-c\left[D\left(k_x^2 + k_y^2 + k_z^2\right) + \mu_a\right]t} \\
& \cdot \Bigg[C\left(k_x, k_y, k_z\right) + \int c\Phi_i\left(k_x, k_y, k_z, t\right) \\
& \underbrace{\cdot G_T\left(k_x, k_y, k_z\right) e^{c\left[D\left(k_x^2 + k_y^2 + k_z^2\right) + \mu_a\right]t} dt}_{\Phi'_e(k_x, k_y, k_z)} \Bigg] \cdot \quad (7)
\end{aligned}
$$

$\Phi_e(k_x, k_y, k_z, t)$ is the Fourier domain representation of $\phi_e(x, y, z, t)$ over spatial dimensions and (k_x, k_y, k_z) is the wave vector. Different from the $\Phi'_e(k_x, k_y, k_z)$ in the confocal system which only includes the characteristics of photon source, here, the $\Phi'_e(k_x, k_y, k_z)$ in the non-confocal system is a represented Fourier field which includes the forward scattered field $\Phi_i(k_x, k_y, k_z, t)$ and object information $G_T(k_x, k_y, k_z)$. Then the temporal boundary of the backward scattered field $\phi_e(x, y, z, t = 0)$, which represents the object, can be obtained by the inverse Fourier transform of its spectrum $\Phi'_e(k_x, k_y, k_z)$. Further, following the key step in the confocal boundary migration model [10], a Stolt interpolation which is based on the dispersion relation $f = c\sqrt{k_x^2 + k_y^2 + k_z^2}$ is used to establish a space-to-time mapping in the frequency domain, where f is denoted as the frequency of light. After the variable change from

k_z to f, (6) can be described as:

$$\phi_e\,(x,y,z,t) = \frac{1}{(2\pi)^3} \int \int \int \overline{\Phi}_e\,(k_x,k_y,f)$$

$$\cdot\, e^{-\left[D\frac{f^2}{c}+c\mu_a\right]t+i\left(k_xx+k_yy+\sqrt{\frac{f^2}{c^2}-k_x^2-k_y^2}z\right)} dk_x dk_y df, \tag{8}$$

where

$$\overline{\Phi}_e\,(k_x,k_y,f)$$
$$= \frac{|f|\,/c^2}{\sqrt{\frac{f^2}{c^2}-k_x^2-k_y^2}}\,\Phi'_e\left(k_x,k_y,\sqrt{f^2/c^2-k_x^2-k_y^2}\right). \tag{9}$$

We note that this interpolation method allows us to convert $\Phi'_e(k_x,k_y,k_z)$ and $\overline{\Phi}_e(k_x,k_y,f)$ without analytically computing them, including their internal functions such as $G_T(k_x,k_y,k_z)$, $\Phi_i(k_x,k_y,k_z,t)$ and $C(k_x,\,k_y,k_z)$. Then, according to the (8), the spatial boundary of backward scattered field $\phi_e(x,y,z=0,t)$, which represents the measurements, can be obtained by 2D Fourier transform over (k_x,k_y) and 1D numerical transform over f of $\overline{\Phi}_e(k_x,k_y,f)$.

Therefore, the operator $A(\cdot)$ establishes the mapping from object $\phi_e(x,y,z,t=0)$ to the measurements $\phi_e(x,y,z=0,t)$ through the interpolation transformation in the frequency domain. Finally, the object reconstruction is the reverse process of the above derivation, as shown in Fig. 2(c). And the pipeline can be summarized as:

$$\phi_e(x,y,z=0,t) \rightarrow \overline{\Phi}_e(k_x,k_y,f) \rightarrow \Phi'_e(k_x,k_y,k_z)$$
$$\rightarrow \phi_e(x,y,z,t=0).$$

The pseudocode of the proposed method is shown in Algorithm 1. The computational complexity of the non-confocal boundary migration model is bounded by the Fourier transform and the numerical transform in (8). Denoting the N as the size of each dimension of measurements, the complexity of the proposed method is $O(N^3 log N)$.

C. Depth Reconstruction Method

The derivation above shows that the depth information of the object is included in the temporal information of measurements $\phi_e(x,y,z=0,t)$. The key step of the depth reconstruction is the temporal numerical transform from $\phi_e(x,y,z=0,t)$ to $\overline{\Phi}_e(k_x,k_y,f)$ over f in (8), which is given by:

$$\phi_e\,(t) = \frac{1}{2\pi}\,\int \overline{\Phi}_e\,(f) \cdot e^{-\left[D\frac{f^2}{c}+c\mu_a\right]t} df. \tag{10}$$

This numerical transform can be discretized as $\phi_e = H\overline{\Phi}_e$, which can be further specified as following:

$$\begin{bmatrix} \phi_e\,(t_1) \\ \vdots \\ \phi_e\,(t_T) \end{bmatrix} = \begin{bmatrix} e^{-\frac{1}{c}\left[Df_1^2+c^2\mu_a\right]t_1} & \cdots & e^{-\frac{1}{c}\left[Df_T^2+c^2\mu_a\right]t_1} \\ \vdots & \ddots & \vdots \\ e^{-\frac{1}{c}\left[Df_1^2+c^2\mu_a\right]t_T} & \cdots & e^{-\frac{1}{c}\left[Df_T^2+c^2\mu_a\right]t_T} \end{bmatrix}$$

Algorithm 1: Non-Confocal Boundary Migration Model.

1: **Procedure** NBMM $(\tau(x,y,t))$
2:    // Initialization
3:     $D = D_0,\ \mu_a = \mu_{a0},\ c = c_0$
4:    // Pre-process data
5:     $\phi_e(x,y,t) = \text{Pre-process}\,(\tau(x,y,t))$
6:    // Construct the transfer matrix over t
7:     $H = e^{-[D\frac{f^2}{c}+c\mu_a]t}$
8:    // Numerical transform over t
9:     $\overline{\Phi}_e(k_x,k_y,f) = H^{-1}\phi_e(x,y,t)$
10:    // Fast Fourier transform over (x,y)
11:     $\overline{\Phi}_e(k_x,k_y,f) = \mathcal{F}_{x,y}(\overline{\Phi}_e(x,y,f))$
12:    // Interpolation
13:     $\Phi'(k_x,k_y,k_z) = \frac{c|k_z|}{\sqrt{k_x^2+k_y^2+k_z^2}}\overline{\Phi}\left(x,y,c\sqrt{k_x^2+k_y^2+k_z^2}\right)$
14:    // Inverse fast Fourier transform
15:     $\phi(x,y,z) = \mathcal{F}^{-1}_{x,y,z}(\Phi'(k_x,k_y,k_z))$
16:    return $|\phi(x,y,z)|$
17: **end procedure**

$$= \begin{bmatrix} \overline{\Phi}_e\,(f_1) \\ \vdots \\ \overline{\Phi}_e\,(f_M) \end{bmatrix}. \tag{11}$$

Since the condition number of temporal transfer matrix H is always large in the practical calculation, the inverse problem of (11) is ill-conditioned, which affects the depth reconstruction ability of the proposed NBMM. To alleviate this problem, we provide a method to recover the depth information.

It can be seen from (11) that the pseudo-inverse matrix of H, denoted as H^{-1}, acts as a weight matrix of the temporal information $\phi_e(t)$ and further determines the depth reconstruction. Then, we analyze weight features of H^{-1} with different matrix sizes. Without loss of generality, the weight difference of the pseudo-inverse matrices H_T^{-1} and H_{T+1}^{-1} with a size of $T \times T$ and $(T+1) \times (T+1)$ is derived, i.e., the matrix size difference ΔT is equal to 1. To analytically describe the matrix H_{T+1}^{-1}, we block the matrix H_{T+1} into four submatrices:

$$H_{T+1} = \begin{bmatrix} H_T & P_1 \\ P_2 & P_3 \end{bmatrix}_{(T+1)\times(T+1)}, \tag{12}$$

where

$$P_1 = \begin{bmatrix} e^{-\frac{1}{c}\left[Df_{T+1}^2+c^2\mu_a\right]t_1} \\ \vdots \\ e^{-\frac{1}{c}\left[Df_{T+1}^2+c^2\mu_a\right]t_T} \end{bmatrix}_{T\times 1},$$

$$P_2 = \begin{bmatrix} e^{-\frac{1}{c}\left[Df_1^2+c^2\mu_a\right]t_{T+1}} & \cdots & e^{-\frac{1}{c}\left[Df_1^2+c^2\mu_a\right]t_{T+1}} \end{bmatrix}_{1\times T},$$

$$P_3 = e^{-\frac{1}{c}\left[Df_{T+1}^2+c^2\mu_a\right]t_{T+1}}.$$

Then, H_{T+1}^{-1} can be calculated according to the block matrix inversion. Taking the leading principal submatrix of order T of the matrix H_{T+1}^{-1} as L_T, we derive the L_T as follows:

$$L_T = H_T^{-1} + H_T^{-1}P_1\left(P_3 - P_2 H_T^{-1}P_1\right)^{-1}P_2 H_T^{-1}. \tag{13}$$
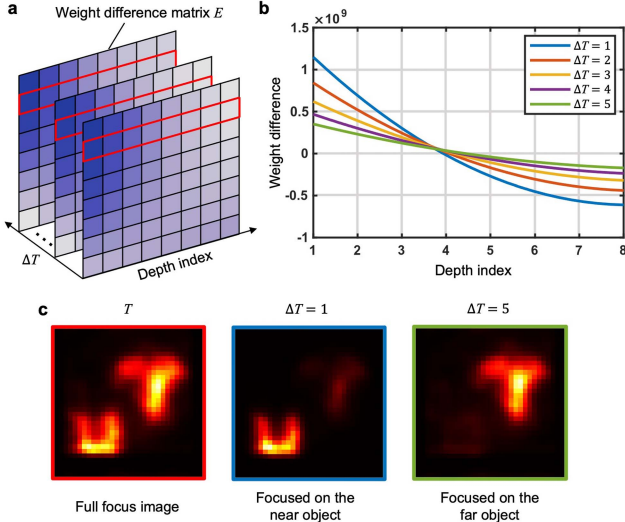
Fig. 3. Instructions of the weight features of H^{-1}. (a) The weight difference matrix E with different matrix size difference ΔT. (b) Taking one row of the matrix E as an example, as shown in (a), the weight difference varies linearly with depth index, which can be used to recover the object at different depths. (c) Using the proposed NBMM with a pseudo-inverse matrix whose size is T, we can obtain the full focus image (marked by red box). Then, changing the matrix size of pseudo-inverse, the reconstructions focused on the near object (marked by blue box) and the far object (marked by green box) can be obtained to recover the object depth information.

And the difference between matrices L_T and H_T^{-1}, denoted as the weight difference matrix E, can be calculated as following:

$$E = L_T - H_T^{-1} = \alpha H_T^{-1} P_1 P_2 H_T^{-1}, \qquad (14)$$

where $\alpha = \left(P_3 - P_2 H_T^{-1} P_1\right)^{-1}$ is a coefficient. Performing numerical analysis of E with different ΔT and taking one row of E as an example, as shown in Fig. 3(a), we obtain the visualized numerical analysis results as shown in Fig. 3(b). The elements in each row of E from left to right represents the weight difference acting on different depths. Thus, the row index of E represents the depth index, as shown in Fig. 3(a). It can be seen from Fig. 3(b) that weight difference varies linearly with the depth index, indicating that the pseudo-inverse matrices with different matrix sizes acting on the temporal information of measurements $[\phi_e(t_1), \ldots, \phi_e(t_T)]$ in (11) give different weights to different depths.

Therefore, we can obtain the reconstruction focused on different depths by changing the matrix size of the pseudo-inverse matrix H^{-1}. Fig. 3(c) shows an example of depth reconstruction. Full focus image (marked by the red box) is obtained by the proposed NBMM using a pseudo-inverse matrix of size T. Then, by changing the matrix size to be $T + 1$ and $T + 5$, i.e., $\Delta T = 1$ and $\Delta T = 5$, we obtain the reconstruction results focusing on the near object (marked by the blue box) and the far object (marked by the green box), respectively, which is consistent with the depth weight difference shown by the curve in Fig. 3(b). Finally, the complete depth information can be recovered by combining the results focused on different depths.

IV. EXPERIMENTAL RESULTS AND ANALYSIS

In this section, we demonstrate the effectiveness of the proposed method. First, a real non-confocal imaging system is built, which is detailed in Section *A*. Then, the experiments under typical static and dynamic scattering scenarios are conducted to verify the imaging ability of the proposed method in different volumetric scattering media. The experimental results are provided in Section *B*, in which the subjective quality and objective evaluation among the proposed method, typical non-confocal scattering imaging methods, and confocal scattering imaging methods are compared. Finally, the imaging limit, the exposure time limit, and comprehensive performance comparison among different methods are analyzed in Section *C*.

A. Experimental Setup

A non-confocal imaging system is designed based on the ultrafast detector array to quickly capture the measurements and verify the proposed method. The hardware prototype is shown in Fig. 4(a). In this setup, a laser (INNO AMT-532-1W1M) is used to emit short pulsed of 12 ps at a wavelength of 532 nm and the laser is driven at a repetition of 20 MHz and 700 mW average optical power. Then a diffuser layer is used to expand the divergence of the laser beam so that it can illuminate the entire scenario. The ultrafast detector of the setup is a single-photon avalanche diode (SPAD) array (Photon Force PF32) with a pixel size of 32×32 and a temporal resolution of 55ps. The detector is equipped with a lens with 2.8-12 mm focal length and 1.6 maximal f-numbers so that the light reflected by the scenario can be focused on the image plane. The laser and detector operate in a non-confocal configuration and they have matched fields of view. A delayer unit (Micro Photon Devices PSD-065-A-MOD) is used to shape the synchronization signal output by the laser into a standard Transistor-Transistor Logic (TTL) signal, which is then used as the acquisition trigger signal of the SPAD array. A data acquisition device (NI-DAQ USB-6343) is used to complete the measurement generation. The reconstruction algorithm is completed by MATLAB software on a desktop computer with a conventional CPU (2.3 GHz Intel Core i5).

B. Experimental Results

To demonstrate the proposed method can operate well in different volumetric scattering scenarios, the polyethylene foam and fog, which are the representative static and dynamic media, respectively, are used. The photos of these two scattering scenarios are shown in Fig. 4(b) and (c). These two scattering media have quite different scattering characteristics and thus produce different scattering responses. The scattering imaging performance of the proposed method and the typical non-confocal scattering imaging methods, time-gating [26], and cross-correlation [21], are compared subjectively and objectively. The depth reconstruction ability of the proposed method is also verified. Additionally, the scattering imaging ability, imaging quality and imaging speed of the proposed method and confocal scattering imaging method [10] are compared. Before running these methods, some pre-processing operations are performed on the
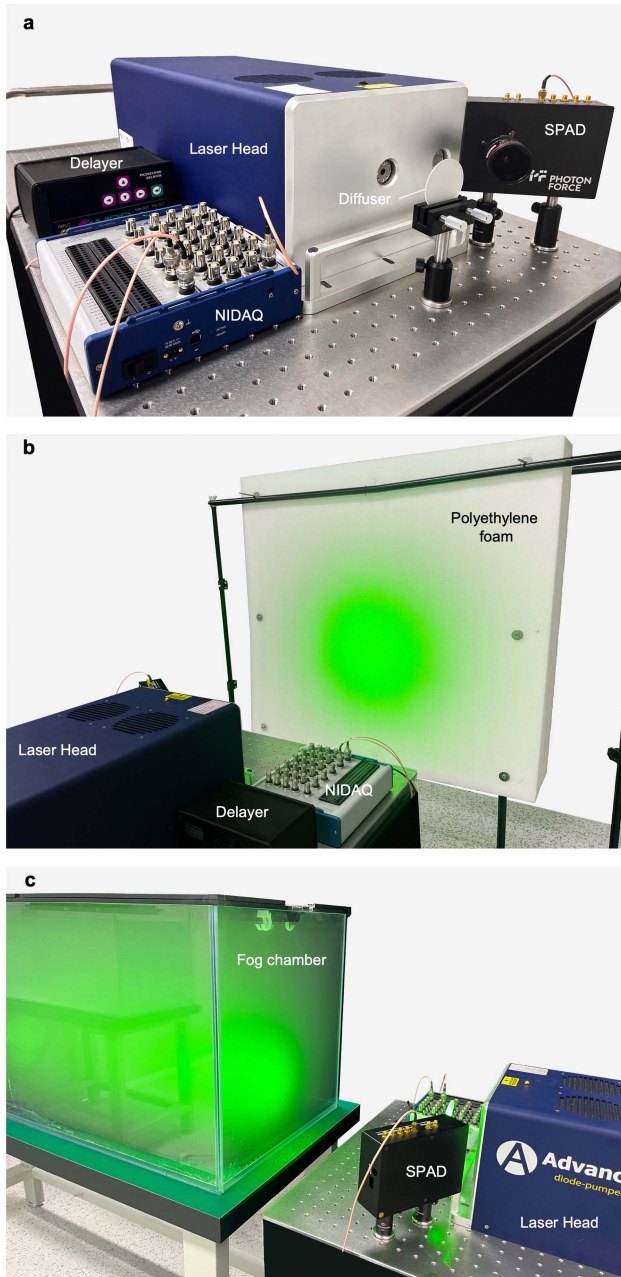
Fig. 4. Hardware prototype of the non-confocal imaging system and typical volumetric scattering scenarios. (a) The setup includes a pulsed laser, a SPAD array detector, a diffuser, a delayer and a data acquisition device. (b) Static scattering scenario: The scattering media is polyethylene foam; the objects are placed between foam slabs of different thicknesses. (c) Dynamic scattering scenario: The scattering media is fog; the object is embedded in the fog; the system illuminates the scenario through the artificial fog chamber made of glass.

measurements, including cropping the photons directly reflected by the surface of the scattering media and rectifying the distance between the scattering scenario and the experimental equipment.

1) Reconstructions Under Static Scenario: Polyethylene foam is used as the static scattering media in this experiment. The characteristics of polyethylene foam are estimated by using an optimal model [10] to minimize the residual between the measurements and theoretical response. Then, the scattering coefficient μ'_s and the absorption coefficient μ_a of the polyethylene foam are estimated as $3.1377 \pm 0.35 \, \mathrm{cm}^{-1}$ and $3.3348 \times 10^{-2} \pm 2.6 \times 10^{-3} \, \mathrm{cm}^{-1}$, which indicates that the length of one TMFP is $l^* = \frac{1}{\mu'_s} = 0.3187 \pm 0.0356 \, \mathrm{cm}$. The test objects include a retroreflective letter 'T' and two two-depth retroreflective letters 'LV' and 'UT'. The objects are embedded in the polyethylene foam at different depths. The depth is defined as the distance between the letter and the front surface of the scattering media and the depth of each letter is marked in Fig. 5(a). Since the object depth is far larger than one TMFP, the signal photons are almost attenuated during the propagation, which makes it challenging to recover the object. Although increasing the exposure time helps capture more signal photons, it results in a long acquisition time. Here, we set the exposure time as 100 ms to achieve rapid object reconstruction.

The measurements and reconstructions generated by time-gating [26], cross-correlation [21], and the proposed method are shown in Fig. 5. It can be seen that the measurements in Fig. 5(b) cannot provide any useful object information in such highly scattering scenarios. The time-gating results in Fig. 5(c) are generated by selecting the corresponding depth gate for the single-depth object or combining multiple depth-shift gates for the multi-depth object [26]. Since decoupling the signal photons from the measurements is difficult, this method fails to recover the object in such a highly scattering scenario. Fig. 5(d) shows the results of the cross-correlation. This method first requires recording the system instrumental response by approximately setting a reference Lambertian target at normal incidence to the axis of the objective lens [21]. Then the results are generated by calculating the cross-correlation between the measurements and the recorded instrumental response. While this method can recover the objects located at a relatively close depth, such as the letter 'U' in data 'UT', the signal-to-noise ratio of the results is low. Besides, the time-gating and cross-correlation methods rely on the object depth prior and the instrumental response prior, respectively. In contrast, our method correctly recovers all targets, as shown in Fig. 5(e), since it makes full use of the ultra-incomplete optical signal and does not require any assumption during the computation. Additionally, we calculate the peak signal-to-ratio (PSNR) of each result to quantitively compare these three algorithms. The ground truth is captured by our non-confocal imaging system without scattering media. And an optimization algorithm is designed to slightly adjust the position of the ground truth so that the reconstructed result can be well aligned with the ground truth and produce maximum PSNR. And all the methods apply this optimization method. Before calculating the PSNR, the ground truth and the reconstructed result are both normalized to [0, 1]. The calculated results are marked in Fig. 5(c)–(e). It can be seen that the proposed method outperforms other methods subjectively and objectively in all experiments.

2) Reconstructions Under Dynamic Scenario: An artificial fog chamber is used to provide a dynamic scattering environment and demonstrate the capability of the proposed method in a time-varying scattering scenario. The size of the fog chamber is $50 \times 50 \times 150$ cm. The transport coefficient μ_t of the fog is estimated as $0.2403 \, \mathrm{cm}^{-1}$ using Beer-Lambert Law. The test
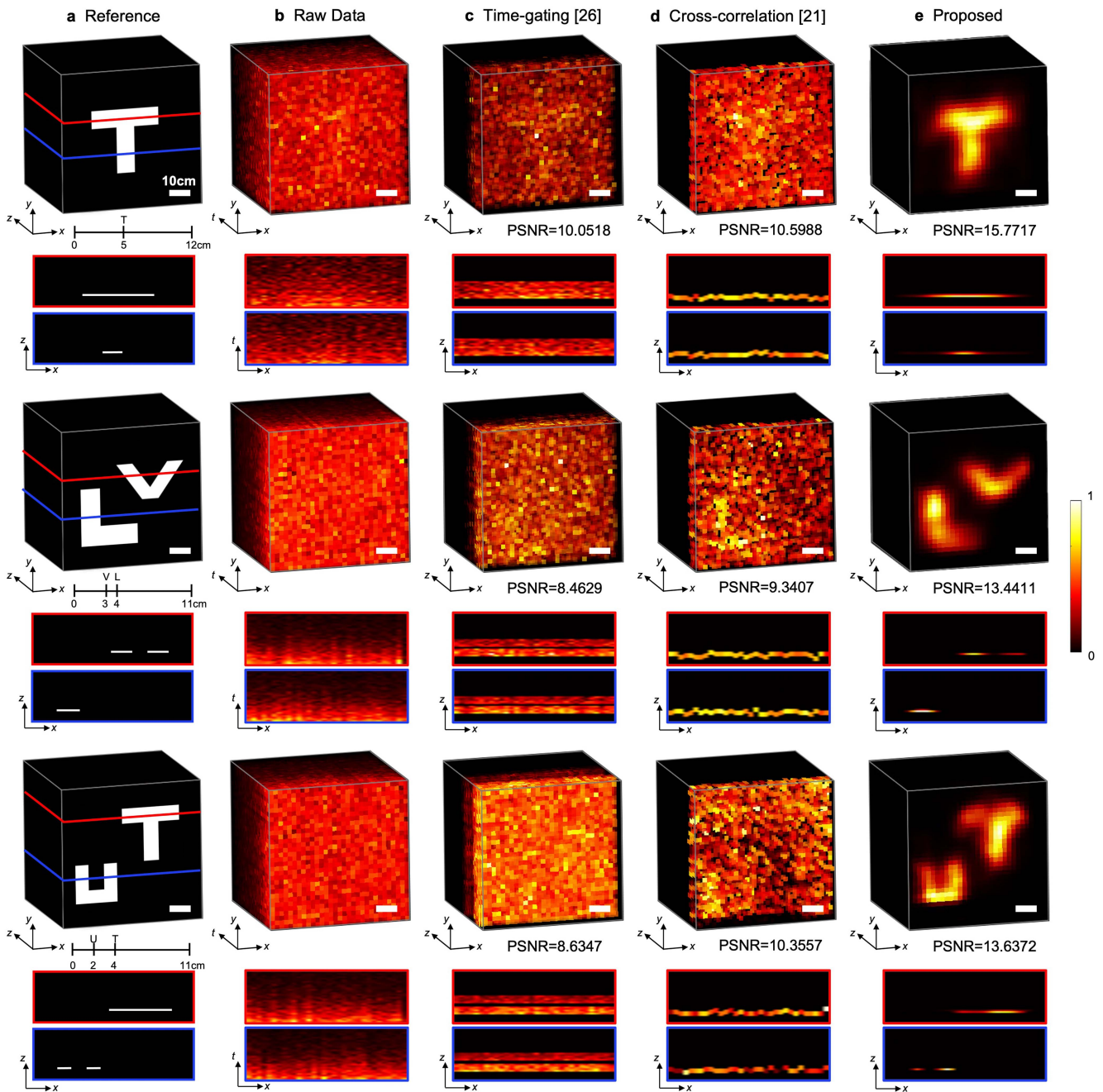
Fig. 5. 3D visualization and x-z slices of reconstructed results in polyethylene foam. (a) Reference of the retroreflective objects used in this experiment. The red and blue lines represent the positions of the x-z slices. The scale bar at the bottom right of each image indicates 10 cm. The total thickness of polyethylene foam and the object depths are marked in the scale below each image. (b) Scattered measurements directly captured by the SPAD array. (c–e) Reconstruction results and x-z slices by time-gating, cross-correlation, and the proposed method, respectively. PSNR is calculated as the quantitative indicator to compare these three algorithms. The results are marked below each image in (c–e), and PSNR is in dB.

objects in this experiment, including 'Vase', 'Mannequin', and 'Bike', have Lambertian surfaces and complex 3D structures, as shown in Fig. 6. The objects are all embedded in the fog and their depth ranges are marked in Fig. 6(a). In this experiment, the exposure time is set as 100 ms.

The measurements and the comparison of the reconstructions by time-gating [26], cross-correlation [21], and the proposed method are summarized in Fig. 6. Since the fog is time-varying, the temporal response is superimposed with dynamic noise. Therefore, the signatures of the objects cannot be distinguished

from measurements as shown in Fig. 6(b), which exacerbates the difficulty of the reconstruction. In this case, time-gating can only provide a fuzzy result with the depth information as a prior, as shown in Fig. 6(c). The cross-correlation method fails to deal with this dynamic case since the system instrumental response is also time-varying and cannot be captured in advance. In contrast, our method is robust in such cases and provides discernible results which have a good qualitative agreement with the ground truth, as shown in Fig. 6(e). PSNR is also calculated as the quantitative evaluator to compare these algorithms. As
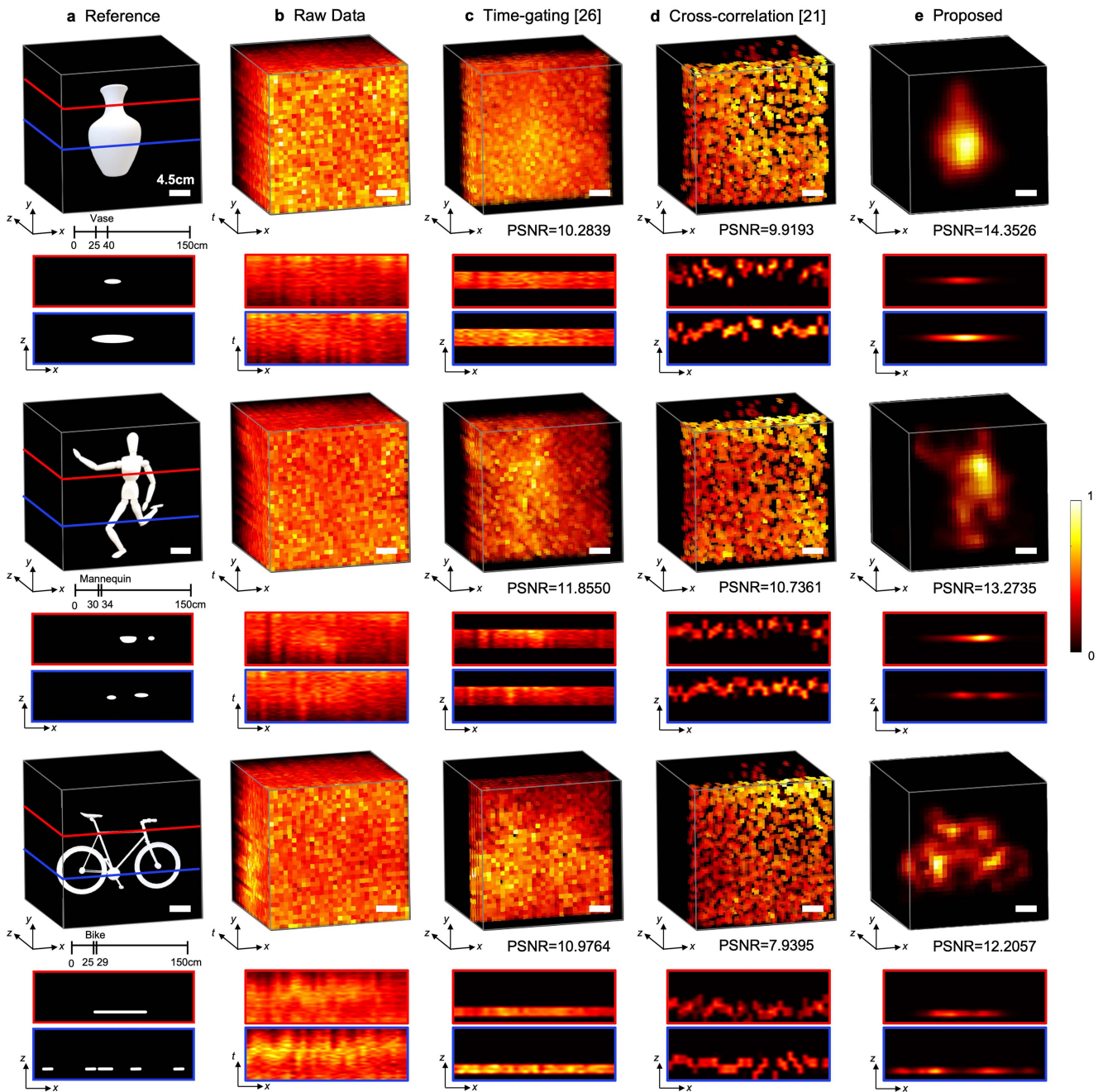
Fig. 6. 3D visualization and x-z slices of reconstructed results in fog environment. (a) Reference of 3D Lambertian objects used in this experiment. The red and blue lines represent the positions of the x-z slices. The scale bar at the bottom right of each image indicates 4.5 cm. The total depth of the fog chamber and the object depths are marked in the scale below each image. (b) Scattered measurements directly captured by the SPAD array. (c–e) Reconstruction results and x-z slices by time-gating, cross-correlation, and the proposed method, respectively. PSNR is calculated as the quantitative indicator to compare these three algorithms. The results are marked below each image in (c–e), and PSNR is in dB.

shown in Fig. 6(c)–(e), our method outperforms time-gating and cross-correlation in all experiments from both subjective and objective evaluation.

3) Depth Reconstructions: The performance of the proposed depth reconstruction method is tested using the measured data in Fig. 5. Following the depth reconstruction method described in Section III, the images focused at different depths can be obtained by changing the size of the transfer matrix H. Then these discretely sampled depth images are combined to recover the 3D structure of the object. The corresponding front views,

top views, and side views of the results are shown in Fig. 7. It can be seen that our method recovers the depth information of the object. As shown in the top view and side view, our method recovers the relative positions of objects at different depths.

4) Comparison of Confocal and Non-Confocal Imaging: The imaging performance, including imaging speed, scattering imaging ability, and imaging quality, of the confocal boundary migration method [10] and the proposed non-confocal boundary migration method is compared in this experiment. First, we summarize the acquisition information of two imaging systems

TABLE I
COMPARISONS OF ACQUISITION INFORMATION OF CONFOCAL AND NON-CONFOCAL IMAGING SYSTEMS

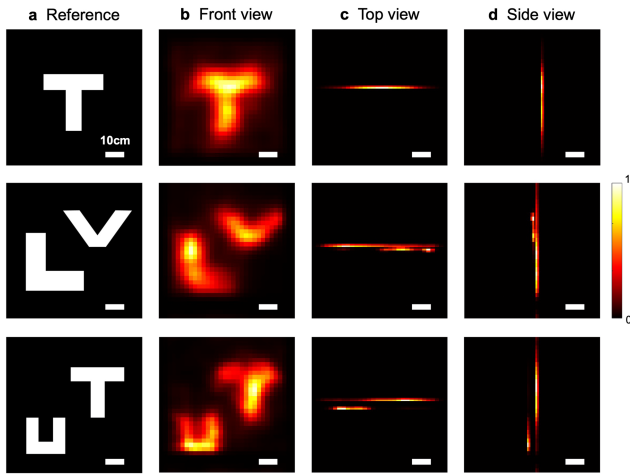| Imaging System	Exposure Time	Scanning Size	Reconstruction Time	Acquisition Time
Confocal	60ms	32×32	120-140ms	61440ms
Non-Confocal	100ms	—	120-140ms	100ms

Fig. 7. Depth reconstruction results. (a) Reference of objects used in this experiment which are the same with the objects in Fig. 4(a). The scale bar at the bottom right of each image indicates 10 cm. (b–d) The front view, top view and side view of the reconstructions.

in Table I. For the confocal scattering imaging system, the measurements are generated by changing the focused point of the laser and detector along a scanning grid. In our previous confocal work [10], the exposure time of each scanning point is set as 60 ms. Since the size of the scanning grid is 32×32, the total acquisition time of each measurement is 61440 ms which is not acceptable for real-time applications. For the non-confocal scattering imaging system, the measurements with a pixel size of 32×32 can be captured by SPAD array with a single exposure. And the exposure time in this experiment is set as 100 ms. It indicates that the total acquisition time of the non-confocal imaging method is 614.4 times shorter than that of the confocal imaging method. Therefore, our non-confocal method can achieve high-speed data acquisition and thus has greater potential for practical scattering imaging scenarios. As for the reconstruction time, since these two methods both have an $O(N^3 \log N)$ computational complexity, they have similar reconstruction speeds. As shown in Table I, the reconstruction time of these two methods to recover a volume of $32 \times 32 \times 128$ voxels is approximately 120-140 ms. The runtime is tested using MATLAB on a conventional CPU (2.3 GHz Intel Core i5).

Additionally, different from the confocal imaging system where the laser power is focused on each scanning point, in the non-confocal imaging system, the laser power is spread out over each pixel, and the number of effective photons reaching each pixel is inversely proportional to the number of SPAD pixels, which further exacerbates the difficulty of the non-confocal reconstruction. In this case, we compare the scattering imaging

capability of these two methods by recovering the retroreflective letter 'T' in the polyethylene foam located at different depths, ranging from 1 cm to 9 cm with an increment of 1 cm. The results are shown in Fig. 8. It can be seen that the confocal imaging method recovers the object located at 28.5 TMFPs. Although the acquisition time of our non-confocal method is 610 times shorter than that of the confocal method, the proposed method successfully recovers the object located at 22.2 TMFPs.

As for the imaging quality, in the valid imaging range of each method, the two algorithms have subjectively similar reconstruction quality. Taking PSNR as the quantitative evaluator, the average imaging quality of the confocal method is 15.8571 and that of the proposed method is 14.9063, as shown in Table II.

In a nutshell, the proposed non-confocal method significantly improves the acquisition time by several hundred orders of magnitude, while reducing the scattering imaging capability by 22% and imaging quality by only 6%.

C. Imaging Performance Analysis

In this subsection, the imaging performance, including the imaging limit and the exposure time limit, of the proposed method and typical non-confocal methods is analyzed and compared.

1) Imaging Limit Analysis: The imaging limit mentioned here refers to the upper limit of the scattering strength quantified by TMFP at which the imaging methods can successfully recover the object. And this indicator is generally given by the experimental tests under different scattering strengths. Therefore, the imaging limits of the time-gating [26], cross-correlation [21], and the proposed method are tested using the built non-confocal imaging system with an exposure time of 100 ms. Fig. 9 shows the reconstruction results of these three algorithms for the target 'T' embedded in the polyethylene foam at different scattering lengths, ranging from 3.2 TMFPs to 28.5 TMFPs. The imaging limit of each method is marked by the green boxes in Fig. 9. It can be seen that time-gating and cross-correlation can only recover the object located at 3.2 TMFPs since they both rely on the ballistic photons which are greatly attenuated and coupled with the scattered photons as the scattering strength increases. In contrast, taking advantage of the accurate non-confocal scattering imaging model and effective reconstruction algorithm, our method improves the imaging limit to 22.2 TMFPs, corresponding to the round-trip scattering length of 44.4 TMFPs.

As for multiple objects with different depths, it can be seen from Fig. 4 that neither time-gating nor cross-correlation methods can handle multiple objects well, while the proposed method can reconstruct multiple objects within an interval of fewer than 6.3 TMFPs. If the interval exceeds this distance,
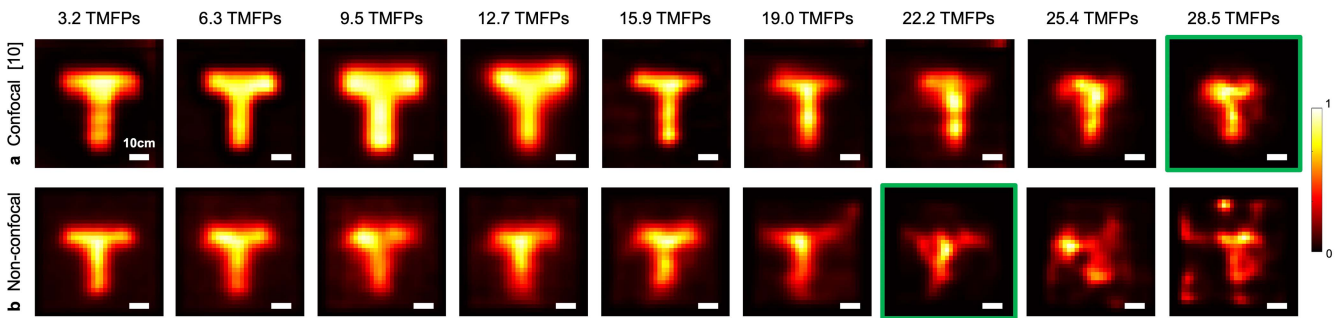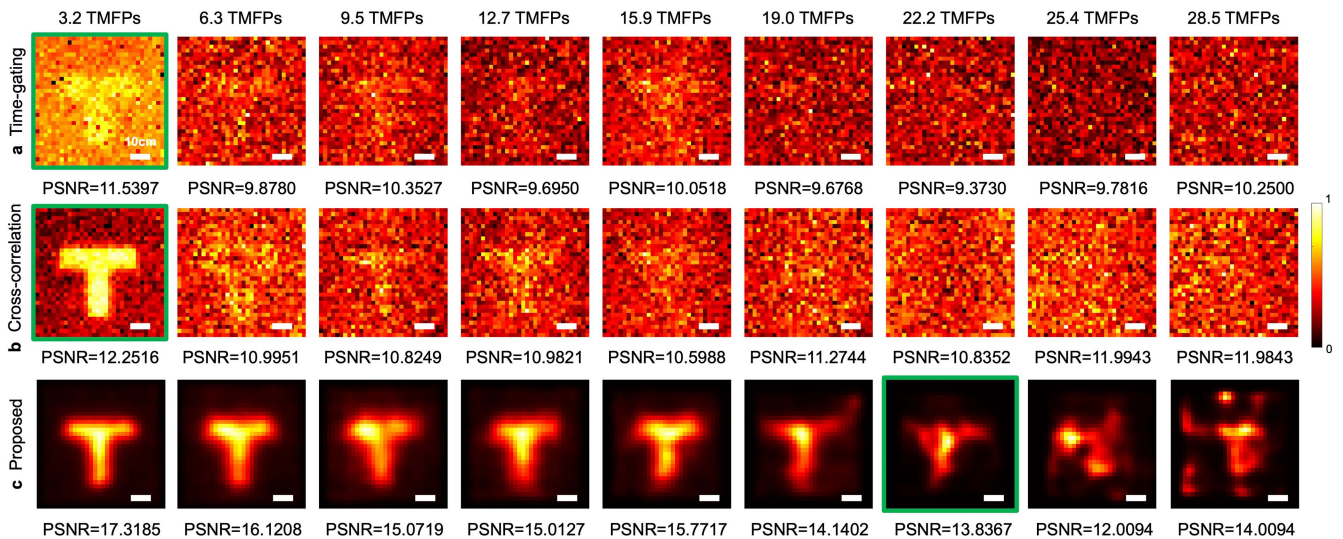
Fig. 8. Reconstructed results of object 'T' located at different depths, ranging from 1 cm to 9 cm with an increment of 1 cm, corresponding to the one-way scattering length from 3.2 TMFPs to 28.5 TMFPs in polyethylene foam. The scale bar at the bottom right of each image indicates 10 cm. (a-b) Reconstruction results by confocal and non-confocal methods, respectively. The green boxes mark the imaging limit of each method.

TABLE II
COMPARISONS OF THE PSNR OF CONFOCAL AND NON-CONFOCAL RESULTS

	Methods	3.2 TMFPs	6.3 TMFPs	9.5 TMFPs	12.7 TMFPs	15.9 TMFPs	19.0 TMFPs	22.2 TMFPs	25.4 TMFPs	28.5 TMFPs	Average
PSNR	Confocal	16.1321	17.0244	15.4982	16.0496	16.4067	16.1077	14.7851	15.2148	15.4950	**15.8571**
	Non-Confocal	17.3185	16.1208	15.0719	15.0127	15.7717	14.1402	13.8367	12.8750	14.0094	**14.9063**

Fig. 9. Reconstructed results of object 'T' located at different depths, ranging from 1 cm to 9 cm with an increment of 1 cm, corresponding to the one-way scattering length from 3.2 TMFPs to 28.5TMFPs in polyethylene foam. The scale bar at the bottom right of each image indicates 10 cm. (a–c) Reconstruction results by time-gating, cross-correlation and the proposed method, respectively. The green boxes mark the imaging limit of each method.

the reconstruction of a more distant object degrades due to signal attenuation and lack of consideration of the multi-bounce transmission between objects.

2) Exposure Time Limit Analysis: To obtain the highest imaging speed of our system, the experiments are conducted with varying exposure times of 1000 ms, 500 ms, 300 ms, 100 ms, 50 ms, and 30 ms. The test object 'T' is located at a depth of 5 cm in the polyethylene foam. The results are shown in Table III. It can be seen that our method can accurately recover the object until the exposure time is less than 30 ms, which is more than 2000 times faster than the confocal method [10]. It means that our method has the potential to observe dynamic

scenes at more than 33 frames per second. While limited by the long storage time of the detector we used in this work, the proposed method cannot achieve such a high frame rate at the current stage. In the future, the development of the hardware or the algorithm design of parallelly processing the acquisition and storage can further accelerate the reconstruction speed to recover moving objects in real time.

Additionally, existing non-confocal scattering methods are compared in terms of exposure time, scattering imaging limit, laser power, and photon counts per pixel. The corresponding indicators described in the respective article are summarized in Table IV. We note that the exposure time discussed above refers

TABLE III
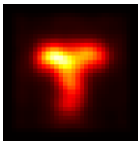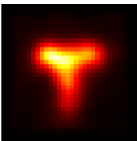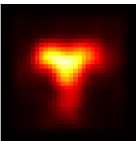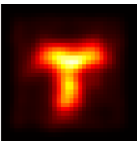COMPARISONS OF THE RECONSTRUCTIONS WITH DIFFERENT EXPOSURE TIMES
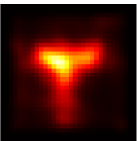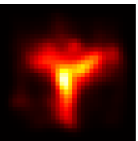
Exposure Time	1000ms	500ms	300ms	100ms	50ms	30ms
Reconstruction						

TABLE IV
COMPARISONS OF DIFFERENT NON-CONFOCAL SCATTERING IMAGING METHODS

| Work	Detector	Pixel Size	Exposure Time	Laser Power	Photon Counts	Object	Prior	Imaging Limit
[Satat et al. 2018]	Photon Force PF32	32×32	2.00s	580mW	20000	3D	Non-prior	4.2 TMFPs
[Maccarone et al. 2019]	COMS SPAD array	192×128	1.00s	8mW	1000	3D	Instrumental response	13.4 TMFPs
[Lyons et al. 2019]	Photon Force PF32	32×32	4.99s	1W	49920	2D	Object depth, media thickness, diffusion coefficient	80.0 TMFPs
[Tobin et al. 2021]	Princeton Lightwave SPAD array	32×32	0.10s	200mW	15000	3D	Non-prior	10.0 TMFPs
Proposed	Photon Force PF32	32×32	0.10s	700mW	10000	3D	Diffusion coefficient	44.4 TMFPs
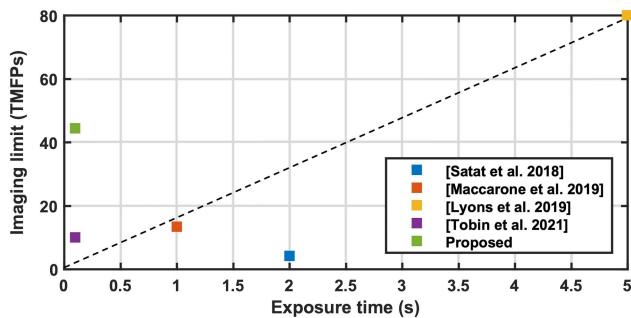
Fig. 10. Comparisons of exposure time and imaging limit of the different non-confocal scattering imaging methods. The dashed line represents the trade-off between exposure time and scattering imaging capability. The method located in the upper left of the dashed line indicates shorter exposure time and higher scattering imaging capability.

to the total exposure time and is given by the product of the photon counts and the exposure time per photon. Therefore, the total exposure time in Table IV indicates the data acquisition time of each method. It can be seen that Maccarone's work [21] requires minimal photons and laser power, but their method cannot deal with highly scattering cases and requires a long acquisition time. Our method and Tobin's work have the fastest acquisition speed, while the imaging limit of our method is 4.44 times more than that of Tobin's work. Besides, the scattering imaging limit in Table IV represents the round-trip scattering length and is uniformly quantified by TMFPs. Fig. 10 visualizes the trade-off between exposure time and scattering imaging limit for these methods. The method located in the upper left of the dashed line has a faster acquisition speed and higher scattering imaging capability. It can be seen that the proposed method and Tobin's work require the shortest exposure time among these

methods. And our scattering imaging capability is also better than most non-confocal works. Although Lyon's work [15] has the highest scattering imaging capability, their method is limited to imaging a simple 2D object and needs prior information on the object depth and the thickness of the scattering media, which limits its ability in practical applications.

V. CONCLUSION

In this article, we provide a non-confocal scattering model and reconstruction methods to address the high-quality and high-speed imaging problem in volumetric scattering media. First, a dual optical coupling scattering transmission model is proposed to accurately describe the forward scattered light propagation and acquisition process using a non-confocal system. Then, a non-confocal boundary migration model is designed to establish a space-to-time mapping in the frequency domain to convert the scattered measurements in spectral form to the object information in the Fourier domain. Additionally, using the characteristic of the temporal transfer matrix, a depth reconstruction method based on depth focusing is developed to recover the 3D information of the object. Since the proposed method makes full use of the ultra-incomplete optical signal and does not require computational approximation, our method recovers the object located at the one-way scattering length of 22.2 TMFPs and presents superior performances among state-of-art methods. Experimental results verify the effectiveness and robustness of the proposed method. Besides, significantly improves the acquisition time by several hundred orders of magnitude, which greatly improves the acquisition speed without large degradation of scattering imaging limit and imaging quality.

REFERENCES

[1] K. He, J. Sun, and X. Tang, "Single image haze removal using dark channel prior," *IEEE Trans. Pattern Anal. Mach. Intell.*, vol. 33, no. 12, pp. 2341–2353, Dec. 2011.

[2] C. Ancuti, C. O. Ancuti, T. Haber, and P. Bekaert, "Enhancing underwater images and videos by fusion," in *Proc. IEEE Conf. Comput. Vis. Pattern Recognit.*, 2012, pp. 81–88.

[3] S. Sudarsanam, J. Mathew, S. Panigrahi, J. Fade, M. Alouini, and H. Ramachandran, "Real-time imaging through strongly scattering media: Seeing through turbid media, instantly," *Sci. Rep.*, vol. 6, Apr. 2016, Art. no. 25033.

[4] G. Satat, M. Tancik, and R. Raskar, "Towards photography through realistic fog," in *Proc. IEEE Int. Conf. Comput. Photography*, 2018, pp. 1–10.

[5] D. Berman, D. Levy, S. Avidan, and T. Treibitz, "Underwater single image color restoration using haze-lines and a new quantitative dataset," *IEEE Trans. Pattern Anal. Mach. Intell.*, vol. 43, no. 8, pp. 2822–2837, Aug. 2021.

[6] D. Berman, T. Treibitz, and S. Avidan, "Single image dehazing using haze-lines," *IEEE Trans. Pattern Anal. Mach. Intell.*, vol. 42, no. 3, pp. 720–734, Mar. 2020.

[7] V. Ntziachristos, "Going deeper than microscopy: The optical imaging frontier in biology," *Nature Methods*, vol. 7, no. 8, pp. 603–614, 2010.

[8] A. T. Eggebrecht et al., "Mapping distributed brain function and networks with diffuse optical tomography," *Nature Photon.*, vol. 8, no. 6, pp. 448–454, 2014.

[9] D. B. Lindell and G. Wetzstein, "Three-dimensional imaging through scattering media based on confocal diffuse tomography," *Nature Commun.*, vol. 11, no. 1, Sep. 2020, Art. no. 4517.

[10] D. Du et al., "A boundary migration model for imaging within volumetric scattering media," *Nature Commun.*, vol. 13, no. 1, Jun. 2022, Art. no. 3234.

[11] B. B. Das, K. M. Yoo, and R. R. Alfano, "Ultrafast time-gated imaging in thick tissues: A step toward optical mammography," *Opt. Lett.*, vol. 18, no. 13, pp. 1092–1094, Jul. 1993.

[12] F. Christnacher, S. Schertzer, N. Metzger, E. Bacher, M. Laurenzis, and R. Habermacher, "Influence of gating and of the gate shape on the penetration capacity of range-gated active imaging in scattering environments," *Opt. Exp.*, vol. 23, no. 26, pp. 32897–32908, Dec. 2015.

[13] A. Maccarone et al., "Underwater depth imaging using time-correlated single-photon counting," *Opt. Exp.*, vol. 23, no. 26, pp. 33911–33926, Dec. 2015.

[14] J. Cho et al., "Time-resolved detection of early-arriving ballistic waves in a quasi-diffusive regime," *Opt. Exp.*, vol. 29, no. 22, pp. 35640–35650, Oct. 2021.

[15] A. Lyons et al., "Computational time-of-flight diffuse optical tomography," *Nature Photon.*, vol. 13, no. 8, pp. 575–579, 2019.

[16] L. Wang, P. P. Ho, C. Liu, G. Zhang, and R. R. Alfano, "Ballistic 2-D imaging through scattering walls using an ultrafast optical Kerr gate," *Science*, vol. 253, no. 5021, pp. 769–771, Aug. 1991.

[17] R. Pierrat, J. J. Greffet, and R. Carminati, "Photon diffusion coefficient in scattering and absorbing media," *J. Oper. Strategic Analytics A*, vol. 23, no. 5, pp. 1106–1110, 2006.

[18] G. Satat, B. Heshmat, D. Raviv, and R. Raskar, "All photons imaging through volumetric scattering," *Sci. Rep.*, vol. 6, 2016, Art. no. 33946.

[19] R. Tobin, A. Halimi, A. McCarthy, P. J. Soan, and G. S. Buller, "Robust real-time 3D imaging of moving scenes through atmospheric obscurant using single-photon LiDAR," *Sci. Rep.*, vol. 11, no. 1, May 2021, Art. no. 11236.

[20] M. Laurenzis and F. Christnacher, "Time domain analysis of photon scattering and Huygens-Fresnel back projection," *Opt. Exp.*, vol. 30, no. 17, pp. 30441–30454, 2022.

[21] A. Maccarone, F. M. D. Rocca, A. McCarthy, R. Henderson, and G. S. Buller, "Three-dimensional imaging of stationary and moving targets in turbid underwater environments using a single-photon detector array," *Opt. Exp.*, vol. 27, no. 20, pp. 28437–28456, Sep. 2019.

[22] R. Tobin, A. Halimi, A. McCarthy, M. Laurenzis, F. Christnacher, and G. S. Buller, "Three-dimensional single-photon imaging through obscurants," *Opt. Exp.*, vol. 27, no. 4, pp. 4590–4611, Feb. 2019.

[23] W. Cai, B. B. Das, F. Liu, M. Zevallos, M. Lax, and R. R. Alfano, "Time-resolved optical diffusion tomographic image reconstruction in highly scattering turbid media," *Proc. Nat. Acad. Sci.*, vol. 93, no. 24, pp. 13561–13564, 1996.

[24] S. R. Arridge and M. Schweiger, "A gradient-based optimisation scheme for optical tomography," *Opt. Exp.*, vol. 2, no. 6, pp. 213–226, 1998.

[25] S. D. Konecky, G. Y. Panasyuk, K. Lee, V. Markel, A. G. Yodh, and J. C. Schotland, "Imaging complex structures with diffuse light," *Opt. Exp.*, vol. 16, no. 7, pp. 5048–5060, 2008.

[26] M. Laurenzis, F. Christnacher, and D. Monnin, "Long-range three-dimensional active imaging with superresolution depth mapping," *Opt. Lett.*, vol. 32, no. 21, pp. 3146–3148, Nov. 2007.

Dongyu Du is currently working toward the Ph.D. degree in control science and engineering with Automation Department, Tsinghua University, Beijing, China. Her research interests include the development of new systems and algorithms for solving problems in scattering imaging, non-line-of-sight imaging, and single-photon imaging.

Xin Jin (Senior Member, IEEE) received the M.S. degree in communication and information system and the Ph.D. degree in information and communication engineering from the Huazhong University of Science and Technology, Wuhan, China, in 2002 and 2005, respectively.

From 2006 to 2008, she was a Postdoctoral Fellow with The Chinese University of Hong Kong, Hong Kong. From 2008 to 2012, she was a Visiting Lecturer with Waseda University, Fukuoka, Japan. Since March 2012, she has been with Shenzhen International Graduate School, Tsinghua University, Beijing, China, where she is currently a Professor. She has authored or coauthored more than 170 conference and journal papers. Her research interests include computational imaging and power-constrained video processing and compression.

She is also the Distinguished Professor of Pengcheng Scholar. She was the recipient of the Gold Medal of International Exhibition of Inventions of Geneva in 2022, the Second Prize of National Science and Technology Progress Award in 2016, first Prize of Guangdong Science and Technology Award in 2015, and ISOCC Best Paper Award in 2010. Dr. Jin is the Member of SPIE and ACM.

Rujia Deng is currently working toward the M.E. degree from Shenzhen International Graduate School, Tsinghua University, Bejing, China. Her research interest include imaging and tracking moving objects in scattering or non-line-of-sight scenarios.